1-21-2004

An Overview of Observations of Unstable Layers during the Turbulent Oxygen Mixing Experiment (TOMEX)

J. H. Hecht
The Aerospace Corporation

Alan Z. Liu
Embry Riddle Aeronautical University - Daytona Beach, liuz2@erau.edu

R. L. Bishop
Clemson University

J. H. Clemmons
The Aerospace Corporation

C. S. Gardner
University of Illinois at Urbana-Champaign

See next page for additional authors

An overview of observations of unstable layers during the Turbulent Oxygen Mixing Experiment (TOMEX)

J. H. Hecht,[1] A. Z. Liu,[2] R. L. Bishop,[3] J. H. Clemmons,[1] C. S. Gardner,[2] M. F. Larsen,[3] R. G. Roble,[4] G. R. Swenson,[2] and R. L. Walterscheid[1]

Received 31 October 2002; revised 15 October 2003; accepted 29 October 2003; published 21 January 2004.

[1] The Turbulent Oxygen Mixing Experiment (TOMEX) was designed to measure the atmospheric response to the existence of unstable layers as determined by wind and temperature measurements from 80 to 105 km. TOMEX combined Na lidar measurements, from Starfire Optical Range in Albuquerque, New Mexico, with a launch of a payload from White Sands Missile Range, located between 100 and 150 km south of Starfire. The payload included a trimethyl aluminum chemical release to measure winds and diffusion, a 5-channel ionization gauge to measure neutral density fluctuations at high vertical resolution, and a 3-channel photometer experiment to measure atomic oxygen related airglow. The rocket was launched when the lidar data indicated the presence of convectively and dynamically unstable regions between 80 and 100 km altitude. For several hours prior to the launch, there had existed a large amplitude atmospheric gravity wave or tide which brought the background atmosphere into being nearly convectively unstable over the 85 to 95 km region. In addition a large overturning in Na density, possibly due to a convective roll, existed at altitudes around 100 km. This type of instability had not been previously seen and identified in this altitude region. The TOMEX payload measured the existence of Kelvin-Helmholz billows, enhanced neutral density fluctuations, enhanced energy dissipation, and well-mixed regions. These features were associated with convectively unstable regions, dynamically unstable regions, convective rolls, and the presence of this large wave. The unstable regions were persistent and covered large vertical (and horizontal regions) of the atmosphere. The atmospheric mixing and energy dissipation appeared to be largely determined by the presence and nature of these instabilities. *INDEX TERMS:* 0310 Atmospheric Composition and Structure: Airglow and aurora; 3332 Meteorology and Atmospheric Dynamics: Mesospheric dynamics; 3379 Meteorology and Atmospheric Dynamics: Turbulence; 3384 Meteorology and Atmospheric Dynamics: Waves and tides; 3394 Meteorology and Atmospheric Dynamics: Instruments and techniques; *KEYWORDS:* composition, mesospheric dynamics, turbulence

Citation: Hecht, J. H., A. Z. Liu, R. L. Bishop, J. H. Clemmons, C. S. Gardner, M. F. Larsen, R. G. Roble, G. R. Swenson, and R. L. Walterscheid (2004), An overview of observations of unstable layers during the Turbulent Oxygen Mixing Experiment (TOMEX), *J. Geophys. Res.*, *109*, D02S01, doi:10.1029/2002JD003123.

1. Introduction

[2] A number of chemical and dynamical processes that have minor significance throughout much of the atmosphere play a major role in determining the structure and energetics at altitudes between 80 to 110 km, often referred to as the MALT (Mesosphere and Lower Thermosphere) region. Absorption of ultraviolet photons by molecular oxygen and the subsequent production of atomic oxygen (O) produces a peak in the atomic oxygen density [O] just below 100 km. The atmospheric densities of [O] and the total gas are high enough so that a number of O-related oxygen airglow emissions occur, resulting in the redistribution of the chemical energy carried by the O atom. The exact position of the [O] peak and the shape of the [O] profile depends on the rate at which O can be transported down to near 80 km where background densities are high enough so that rapid recombination of O + O + M occurs [e.g., *Garcia and Solomon*, 1985; *Roble and Ridley*, 1994], where M represents any atmospheric species. The processes that control that transport are dependent on bulk vertical motions (vertical wind) and diffusion processes [*von Zahn et al.*, 1990]. Vertical winds and transport can be influenced by large scale global circulation patterns, but also locally by the magnitude of the dominant tides, atmospheric gravity waves (AGWs), and the interactions of waves and tides

[1]Space Science Applications Laboratory, The Aerospace Corporation, Los Angeles, California, USA.
[2]Department of Electrical and Computer Engineering, University of Illinois, Urbana, Illinois, USA.
[3]Department of Physics and Astronomy, Clemson University, Clemson, South Carolina, USA.
[4]National Center for Atmospheric Research, Boulder, Colorado, USA.

0148-0227/04/2002JD003123$09.00

[e.g., *Schoeberl et al.*, 1983; *Walterscheid et al.*, 1987; *Angelats i Coll and Forbes*, 1998; *Hickey et al.*, 2000; *Hickey and Walterscheid*, 2001]. Waves also perturb the background horizontal winds and temperature. As the wave amplitude grows with altitude, eventually the perturbations are large enough to cause wave breakdown via the production of convective and/or dynamical instabilities. These instabilities can produce enhanced mixing resulting in an increase in the effective diffusion rate. The MALT region is thought to be a region where significant wave breakdown occurs [see, e.g., *Hodges*, 1967; *Hodges*, 1969; *Lindzen*, 1981; *Schoeberl et al.*, 1983; *Garcia and Solomon*, 1985; *von Zahn et al.*, 1990; *Fritts et al.*, 1997; *Hecht et al.*, 1997; *Gardner et al.*, 2002]. Processes such as the mixing due to turbulent wave breakdown can occur rapidly. However, as *von Zahn et al.* [1990] point out, once mixed, the unmixing can also take days. Because until recently it was not possible to probe the MALT region at sufficient temporal and spatial resolution, some of what is described above was based on modeling.

[3] In particular, an important question not addressed is how the species present in the MALT region are actually affected when potentially unstable conditions occur. For a number of years several techniques were used to try to address this question. In situ measurements of the MALT region using rocket probes have the longest history. One popular technique was using a chemical release to allow a photographic measurement of the winds [*Larsen*, 2002]. This technique has an almost 50 year history and indeed billows presumably due to a Kelvin-Helmholz type unstable shear layer have been observed [e.g., *Lloyd et al.*, 1973]. However, very rarely if at all are simultaneous temperature measurements made in order to accurately determine the Richardson number, R_i, which is the indicator of whether an instability should exist [*Richardson*, 1920; *Gossard and Hooke*, 1975]. Furthermore, temporal information is not available prior to the launch so the time history of the potentially unstable region does not exist.

[4] To overcome some of these problems, several multi-instrument rocket campaigns were carried out at mid and high latitudes from 1983 to 1990. These included, among others, the MAP/WINE campaign in 1983 [*von Zahn*, 1987], the ROSE campaign in 1988/89 [*Rose et al.*, 1992], and the DYANA campaign of 1990 [*Offermann*, 1994]. During these campaigns newly developed instruments such as high-sensitivity ionization gauge and plasma density probes were flown on a number of rocket flights. These instruments made it possible to measure neutral density fluctuations at spatial resolutions approaching 10 m. From these data one could derive, in principle, the turbulence spectrum, the eddy diffusion coefficient, the temperature profile, and the presence of short vertical wavelength gravity waves. When additional measurements were made to measure the horizontal winds, using chaff for example, one could also determine regions where AGWs were convectively and/or dynamically unstable. The results from these campaigns were summarized in a number of papers [*Thrane et al.*, 1987; *Lübken et al.*, 1987; *Blix et al.*, 1990; *Friker and Lübken*, 1992; *Thrane et al.*, 1994; *Lübken et al.*, 1994; *Hillert et al.*, 1994; *Lehmacher and Lübken*, 1995] and produced a number of important results. AGWs were often seen in regions of negative or low ($\ll$1) Richardson number indicating that a dynamical ($0 < Ri < 1/4$) and/or convective instability ($Ri < 0$) existed. These unstable regions were mostly regions where increased turbulence existed. Enhanced eddy diffusion was associated with these unstable regions. In fact, the turbulence was localized within unstable regions [*Lehmacher and Lübken*, 1995] consistent with some of the ideas presented by *Fritts and Dunkerton* [1985]. Turbulent regions and unstable regions were identified in over 90% of the flights.

[5] Despite the great successes of these campaigns there were a number of uncertainties, as discussed by the various authors cited above. (1) Even if all the in situ measurements were perfectly accurate and complete, they only represented a snapshot in time; i.e., there was no way of knowing without supporting ground-based measurements, for example, how long instability regions existed before the rockets were flown. (2) Complete supporting wind and temperature measurements were often not available even at the time of the launch and never available with sufficient accuracy prior to the launch to measure the time history of the instability. (3) Many of the ionization gauge data were only available up to 90 km, yet good temperature measurements required density data up to 110 km in order to derive temperatures in the 90 to 100 km free molecular regime, the only altitudes where this technique was truly applicable. Even then, temperature uncertainties were often quite high, precluding a good estimate of unstable temperature regions. Good atmospheric temperature lidars were not then routinely available. (4) Wind data were often not available at the time of the launch and never using the chemical release method. Na wind lidars were also not available for these experiments.

[6] In the mid 1990s a state-of-the-art Na wind temperature lidar was placed at the 3.5 m Starfire Optical Range telescope in Albuquerque New Mexico. This instrument was capable of measuring temperatures and winds at about 100 m resolution over a few minute integration time so that accurate Richardson numbers could be determined over the nominal 80 to 105 km sensitivity range of a Na lidar. The data obtained from this instrument showed that at this location both convectively and dynamically unstable regions were quite common, occurring sometime in that altitude range almost nightly [*Gardner et al.*, 2002; *Zhao et al.*, 2003]. The location of this instrument was only a short distance from the White Sands Missile Range. The Turbulent Oxygen Mixing Experiment (TOMEX) was planned to take advantage of this location.

[7] TOMEX was a coordinated lidar sounding rocket experiment whose objective was to measure the atmospheric response of the MALT region to the prior existence of either convectively or dynamically unstable regions. In operation the Starfire lidar measured the wind and temperature profiles and determined when convectively or dynamically unstable regions occurred. Within an hour after regions appeared an instrumented sounding rocket was launched. The rocket was a mother-daughter payload with a chemical release in the mother section, and 3 photometers and 5 ionization gauges in the daughter payload section. The daughter payload was ejected near 70 km. The instrumented payload made measurements of (1) the winds, eddy diffusion, energy dissipation rates, and the existence of turbulent billow structures which result from unstable layers on the upleg and downleg from 80 to

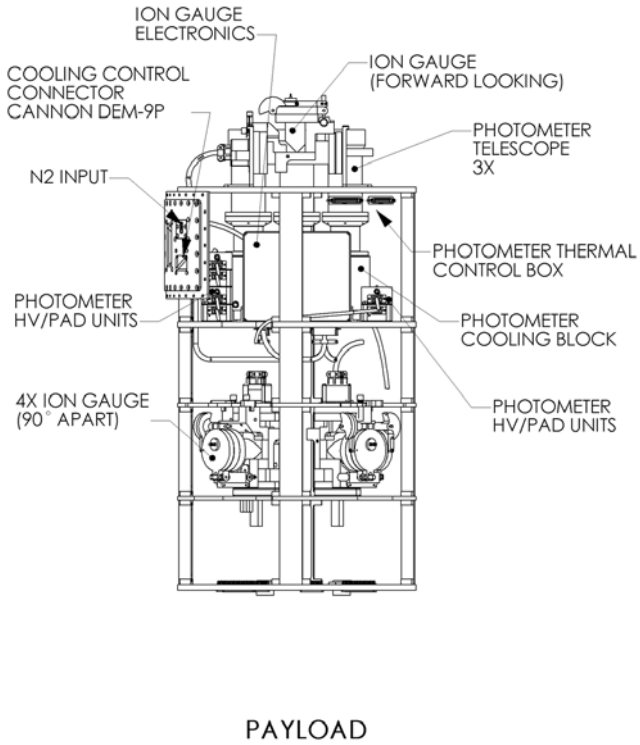

Figure 1. A schematic view of the TOMEX instrumented daughter payload.

120 km using the chemical release, (2) the existence of turbulent layers as evidenced by neutral density fluctuations measured by the ion gauges, and (3) the vertical profile of atomic oxygen derived using O-dependent airglow emissions measured by the photometers.

[8] While other papers in this topical section include detailed results from the ground-based and rocket-based investigations, this paper includes an overview of the results from all the measurements. Here we discuss when and how long the MALT region was unstable, how the atmosphere responded, and the extent to which the various mechanisms (instabilities or eddy mixing) contribute to this response.

2. Experimental Instrumentation and Models

[9] The TOMEX experiment consisted of a Black Brant VB sounding rocket (NASA rocket 21.126) launched from the Sulf Site launcher (33.72 N,106.74 W) at the northern edge of White Sands Missile range in New Mexico, and supporting ground based imaging and lidar measurements made from Starfire Optical Range (34.96 N,106.46 W) about 140 km to the north. The sounding rocket resembled that flown during Coqui Dos [*Hecht et al.*, 2000] in that it consisted of a mother daughter payload on a Black Brant V. The TOMEX mother payload included a chemical release while the daughter payload included a 5-channel ionization gauge (IG) experiment and 3-channel photometer experiment. Figure 1 shows the instrumented daughter payload.

[10] The TOMEX sounding rocket was launched at 0957 UT on 10/26/00. The daughter payload was ejected above 65 km at a separation of a few m/s. It traveled at about 1 km/s through the 80 to 110 km region with a spin rate of almost exactly 1 Hz. The rocket was pointed within a few degrees of zenith and maintained that pointing within 0.1 degrees through the 80 to 105 km region of interest on the upleg. The rocket pointed downward on the downleg so as to provide favorable measurement conditions for the IGs. Since the experiment was designed to measure the response of the atmosphere a five position lidar pointing scheme, described below, was adopted. Figure 2 shows the relative position of

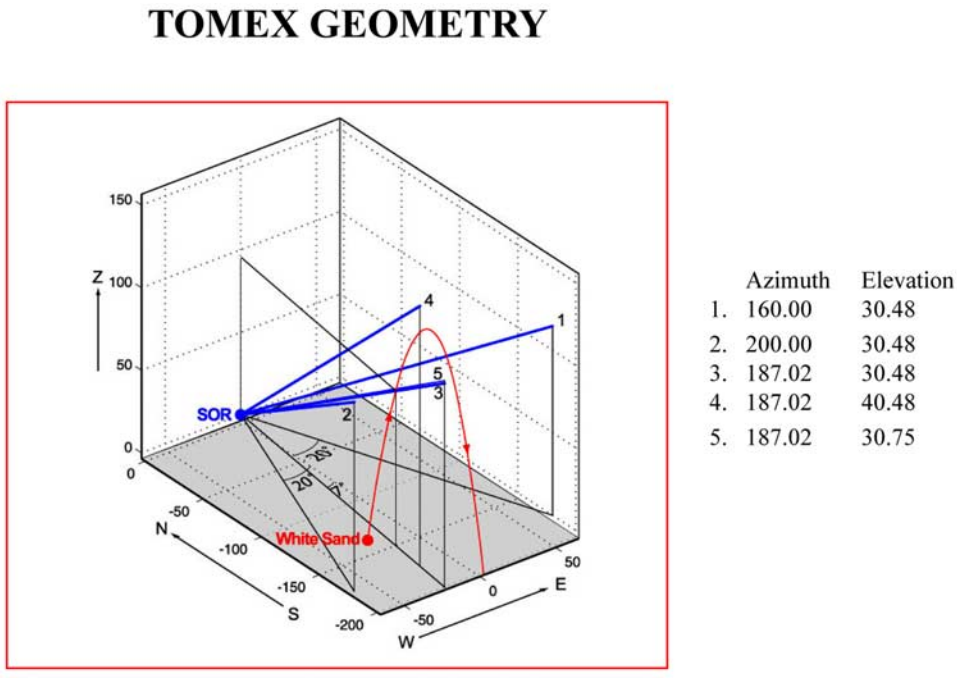

Figure 2. A 3-D schematic view of the TOMEX trajectory and the lidar pointing positions. The distances are in kilometers, and SOR represents the position of the Starfire Optical Range.

the lidar and the rocket trajectory. The three rocketborne experiments are described next followed by a description of the ground-based instruments. Further and more complete information about the data from these instruments and the instruments themselves can be found in the work of *Hecht et al.* [2004], *Larsen et al.* [2003, 2004], and *Bishop et al.* [2004].

2.1. 3-Channel Photometer

[11] To measure atomic oxygen related airglow and also infer atomic oxygen density profiles a 3-channel forward looking photometer included filters at (1) 762.0 nm to record the (0, 0) O_2 Atmospheric (hereafter O2A) band, (2) 773.5 nm to record the (9, 4) OH Meinel (hereafter OHM) band, and (3) 557.0 nm to measure the OI greenline emission. The O2A (0, 0) filter had a FWHM (full-width at half maximum) of 8 nm, the OHM (9, 4) filter had a FWHM of 5 nm, and the greenline filter had a FWHM of about 2 nm. Data points were obtained every 25 ms, and the rocket velocity through the 80 to 100 km region of interest was near 1 km/s. The difference in integrated signal before entering the airglow emission layer (nominally at 80 km) and after leaving the layer provides the integrated brightness of each airglow emission in Rayleighs. The data are also smoothed over about 1 to 2 km in altitude, depending on the filter, and then differentiated over about 1 to 2 km to give volume emission rates. For the O2A filter there is minimal contamination from some weak OH lines which is corrected for by scaling the data from the OHM (9,4) filter following *Mies* [1974]. The O2A and greenline airglow data can be inverted following *McDade et al.* [1986] to determine the [O] profile. This was previously done for the O2A data from the similar instrument flown during Coqui Dos [*Hecht et al.*, 2000]. All data were corrected for the van Rhijn effect [*Chamberlain*, 1961].

2.2. Ionization Gauges

[12] An ionization gauge experiment was included in the TOMEX payload in order to characterize the neutral atmosphere at small scales. The primary impetus was to measure neutral density fluctuations associated with unstable regions. As shown in Figure 1, the instrument utilized five sensors oriented at various angles in order to sample a variety of flow conditions. The instrument is very similar to that used for analysis of the flow fields associated with ionospheric sporadic E (J. H. Clemmons et al., In-situ techniques for aeronomy using multiple ionization gauges, submitted to *Journal of Atmospheric and Solar-Terrestrial Physics*, 2000). Each sensor consisted of a commercially available miniature pressure gauge sensor, used typically to measure low pressures in ground-based vacuum chambers, coupled to an accommodation chamber. The chamber was sealed before launch and opened by breaking the seal once the payload attained altitude. The theoretical time constant of this system was a few milliseconds. Electronics inside the payload provided the circuitry to control and measure the emitted electron current as well as to measure the collected ion current. High-resolution, high-speed analog-to-digital converters were used in order to provide rapid (1 kHz) measurements spanning a large dynamic range (20 bits) in pressure. During the flight good data were obtained with better than 10 m vertical spatial resolution.

[13] For this paper relative neutral density fluctuations are calculated from the data. The term "relative" means that they are the result of subtracting the actual measurements from a long-baseline detrend, then normalizing to the value of the detrend. Similar techniques have been performed on ionization gauge data by *Lübken et al.* [1994] and by *Blix et al.* [1990] on their neutral and ion probe measurements. The results presented are rather insensitive to that actual form of the detrend, but the method used is as follows. First several spins of data were fitted to a power law in altitude to give a smooth function. The data were normalized by this function and then the residual spin tone (about 1% of the total signal) was removed by fitting every spin to a constant plus a sinusoid. This function was then used to normalize the data once again. Departures of the renormalized data from one are then taken to be relative density fluctuations. These residuals are then essentially the ratio of a high-pass filtered portion of the signal to a low-pass portion.

2.3. TMA Chemical Release

[14] To provide winds, horizontal eddy diffusion and energy dissipation [*Rees et al.*, 1972], and 3-D views of turbulent structures such as KH billows, a chemical release technique was used on TOMEX that has been described extensively in the literature [see, e.g., *Larsen*, 2000a, 2000b, 2002]. Trimethyl aluminum (TMA) trails were released on the upleg and downleg portions of the flight. TMA reacts with oxygen to produce a chemiluminescence that makes it possible to track the trails photographically over a period of tens of minutes. By using the star background and photographs from two or more sites, the location and movement of the trail were determined, and the wind, diffusion and energy dissipation profiles could be determined. The triangulation was carried out with observations from SOR, from the VLA radio astronomy site, and from the Sunspot solar observatory site. The chemical release module was on the mother portion of the payload and incorporated a solenoid valve system to modulate the release and a regulated nitrogen supply to control the mass released in each puff. The puffs were 1 s duration and 2 s delay between puffs. This allowed a measure of vertical diffusion as well as horizontal diffusion and energy dissipation rates. However, the puffs limited the vertical resolution to 1 km. The typical accuracy for the measured winds is a few meters per second [*Larsen et al.*, 1989].

2.4. Na Wind and Temperature Lidar

[15] Nearly simultaneous temperature and wind data were obtained from the University of Illinois Na Wind/Temperature lidar system [*Bills et al.*, 1991; *Gardner and Papen*, 1995] located at Starfire Optical Range. This lidar technique derives wind and temperature by probing the width and center frequency of the Na D2 absorption line, which are functions of wind (Doppler shift) and temperature (thermal broadening). By taking advantage of the Starfire 3.5 m telescope this lidar system can measure winds and temperature with an uncertainty of a few m/s and a few K at better than 100 m vertical resolution with 90 s integration time. As shown in the work of *Zhao et al.* [2003] and [*Gardner et al.*, 2002], the sensitivities of these measurements are just good enough for reliable estimation of the

dynamical and convective instabilities. For this work the lidar obtained densities every 24 m but these are averaged and the resultant 96 m bins are used.

[16] For TOMEX, the lidar operated in a 5-position mode as illustrated in Figure 2. The 5 positions P1 to P5 were designed to probe the volume of atmosphere around the rocket trajectory. At each position, line of sight wind, temperature and Na density along the lidar beam were obtained with an integration time of 90 s. It took less than 30 s to move the telescope to the next position. The primary position P3 has an elevation angle of 30.48° and an azimuth of 187.0°. The lidar beam at this position intercepted the upleg rocket trajectory at 95 km, which was about 153 km in horizontal distance from SOR. Two other positions, P1 and P2 had the same elevation angle as P3 but with azimuth of 160° and 200°, respectively. These two beams were designed to measure the two horizontal wind components. P4 and P5 had the same azimuth angle as P3. The elevation angle of P4 is 10° higher than P3. It was designed to measure the north-south gradient. P5 was 1 km above P3 at the intersection point with the rocket upleg trajectory. It was designed to measure the vertical gradient.

2.5. Ground-Based Imaging and Spectroscopy of OHM

[17] An airglow imager, located at Starfire, measured mesospheric OH (750.0–930.0 nm with a notch at 865.0 nm) and O2 Atmospheric band emissions (865.0 nm). A single image observes waves with horizontal wavelengths <300–400 km over a field of view of approximately 300–400 km, including the White Sands missile range. For wavelengths >300 km, temporal analysis of zenith observations are performed. Quasi-monochromatic (QM) waves have been analyzed for their intrinsic parameters [*Swenson et al.*, 1999; *Haque and Swenson*, 1999]. Spectral methods of recovering the angular, power spectra as well as momentum flux from time motion analysis [*Coble*, 1997; *Coble et al.*, 1998; *Gardner et al.*, 1999] have been used to analyze these data. A Michelson interferometer observed the zenith sky at Starfire in the OH (3–1) and (4–2) bands and OH intensity was calculated.

2.6. Model

[18] TIME-GCM [*Roble and Ridley*, 1994] is a self-consistent model with complete chemistry. In this work it was run using input parameters appropriate to the TOMEX period. Data extracted from the model and used in this work were the total density, the constituent densities, the temperature, winds, and the predicted airglow emission profiles.

[19] The model data were used extensively in the work of *Liu et al.* [2004] and *Hecht et al.* [2004]. The former study was interested in seeing how closely the tides were fit so the model was also run using new tidal forcings from *Hagan and Forbes* [2002]. These tidal forcings gave a good but not perfect fit to the observed tidal amplitudes as described below and in the work of *Liu et al.* [2004]. The *Hecht et al.* [2004] study was interested in how eddy diffusion affected the model output so eddy diffusion was varied as an input to the model using the standard tidal forcings. The model outputs were then used as the background atmosphere and the perturbation in these backgrounds were calculated due to an enhanced tide or gravity wave following *Walterscheid et al.* [1987] and *Walterscheid and Schubert* [1995] as discussed in the work of *Hecht et al.* [2004].

3. State of the Atmosphere Prior to and Around the Launch

[20] The state of the atmosphere on this night is discussed in much more detail by *Liu et al.* [2004] and specifically with respect to the Na density data by *Larsen et al.* [2004]. Figure 3 gives an overview of the data obtained by the lidar over the entire evening for the Na density, temperature, and winds. They all show contour plots which are smoothed over 1 km in altitude. While data from P3 are shown for temperature and Na density, all positions showed similar features suggesting that they extend horizontally over many tens to possibly hundreds of kilometers.

[21] There are several interesting aspects of the Na density data near the time of the launch. The main feature was a large peak below 90 km. Some small-scale structure also existed. In particular, as seen more easily in the line plots shown in the work of *Liu et al.* [2004], there was a small wavelike structure, near 90 km, with a vertical scale of a few km or less.

[22] However, the most interesting feature in these density data occurs above 95 km where there was a large vertical upwelling of Na. The origin of that upwelling earlier in the night is discussed in more detail by *Larsen et al.* [2004]. They summarized the observations of the overturning feature seen in the Na density data as follows. It had a timescale of several hours and a vertical scale of 5 to 6 km. The region of the overturning was characterized by low stability, with much higher stability capping the top of the feature where the temperature began to increase rapidly at the base of the thermosphere. The wind profiles show an inflection point in the meridional winds near the middle of the overturning height range. There was a large shear in the zonal wind in the same altitude range which further decreased the stability. The characteristics of this feature indicate that is not caused by either a convective or a Kelvin-Helmholz instability. However, its characteristics are similar to those found in convective rolls which are commonly seen in the lower atmosphere boundary layer region. The exact dynamics causing such rolls to appear in the upper atmosphere has yet to be determined though.

[23] The temperature data appear to be without any steep gradients prior to about 7 UT. After that time, peaking around 1000 UT a wavelike feature with vertical wavelength near 20 km, possibly due to a tide or combination of a tide and AGW, was present producing a steep negative temperature gradient from 85 to almost 95 km as evidenced by the closely spaced contours. Just before the launch the minimum temperature occurs around 95 km. The line plot at 0955 UT, presented in the work of *Liu et al.* [2004], shows some short vertical structure, similar to that seen in the Na density, just below 90 km which also seems to have a short (few km or less) vertical wavelength. Additional short vertical structure existed between 95 and 98 km.

[24] The meridional wind data, which are essentially the line of sight winds and therefore show low noise, indicates that there was a shear present for many hours prior to

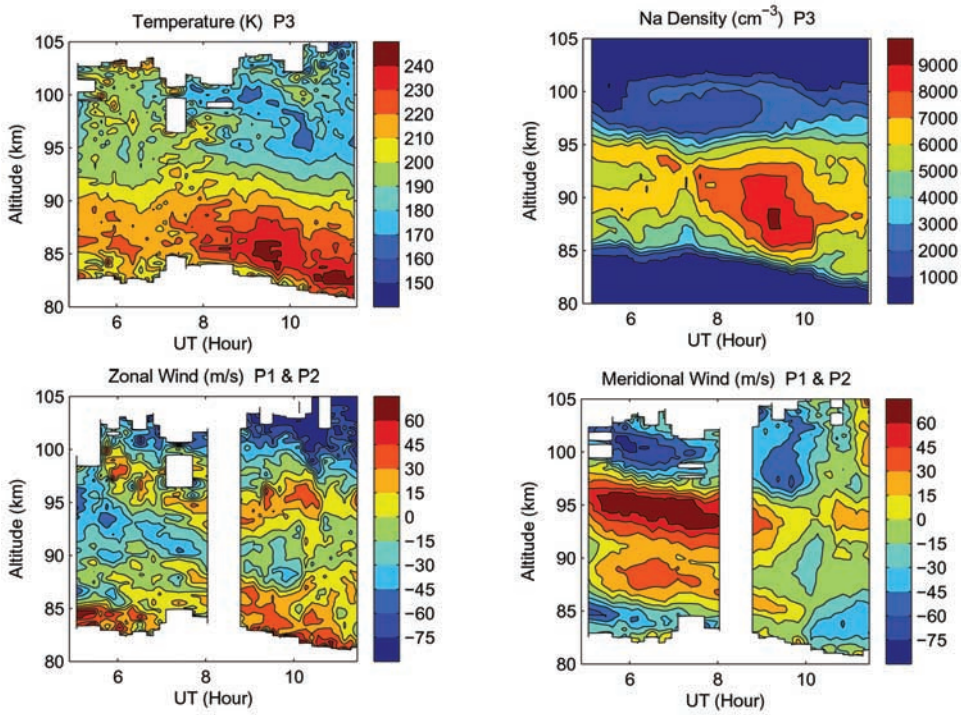

Figure 3. Contour plots of Na density, temperature, meridional, and zonal wind as a function of time and altitude from the Starfire lidar data. The data have been smoothed over 1 km.

1000 UT in the region between 95 and 100 km. That shear however was dissipating at the time of the launch.

[25] The zonal wind data, which are noisier, show a shear region near 87 km that was present for most of the hour prior to launch. Above 100 km a zonal shear also was present.

[26] Two main features are of interest here: (1) large temperature gradients that exceed the adiabatic lapse rate (about 9.5 K/km in the MALT region) can produce a convective instability (Ri < 0), and (2) large magnitude wind shears (nominally exceeding 40 m/s/km) which when combined with the temperature gradient can produce values of Ri less than 1/4, the nominal onset of a dynamical instability.

[27] Ri is given more formally by

$$Ri = \frac{(g/T)\left(dT/dz + g/C_p\right)}{(du/dz)^2 + (dv/dz)^2}, \qquad (1)$$

where as a function of altitude z, g is the acceleration due to gravity, T is the temperature, u and v are the zonal and meridional wind speeds, and C_p is the atmospheric specific heat at constant pressure. Thus the numerator is the square of the Brunt-Vaisala frequency, N^2. In the MALT region N^2 is about 0.0004 sec^{-2} [e.g., *Hecht et al.*, 1997] so that wind shears greater than about 40 m/s/km are typically needed for a convective instability.

[28] *Liu et al.* [2004] derive shears and temperature gradients calculated using the data from P1 and P2. The largest shears on this night were at 86 to 87 km, predominantly due to the zonal wind, and at 95 to 97 km, predominantly due to the meridional wind. The latter had magnitudes exceeding 40 m/s/km from about 0600 UT, and still have a narrow region exceeding that value at just before the launch. However, Ri also depends on the temperature gradient. There was a large negative temperature gradient near or above the adiabatic lapse rate from about 86 to 94 km for much of the hour before the launch. Thus, even if N^2 is not less than zero, producing a convective instability, a low value of N^2 would mean that a much smaller than normal wind shear is needed to produce a dynamical instability. Thus in the 85 to 95 km region some type of instability becomes likely. However, in the region above 95 km the temperature gradient was sometimes positive making a dynamical instability less likely.

[29] Figure 4 shows plots of N^2 and Ri derived from the data and discussed more fully in the work of *Liu et al.* [2004]. Note that these results are essentially independent of which lidar position is used. The N^2 plots show narrow regions where N^2 was less than zero between 86 and 94 km in the hour before the launch. Some also show isolated regions between 95 and 100 km where N^2 was less than zero. The instability regions do appear to have occurred in narrow layers. Between 9 and 10 UT almost the entire 86 to 94 km altitude range had N^2 below zero at some point in time indicating a convective instability. The fact that all four show these potentially unstable regions suggest they are real. These data do confirm that much if not all of the 86 to 94 km region had undergone a convective instability at some point between 9 and 10 UT. In addition the data indicate that at the time of the launch the region at 90 km was convectively unstable. The region around 93 km could also have been convectively unstable. Slightly before launch at about 0930 UT regions with small but positive N^2, conducive to dynamical instabilities, existed throughout the 86 to 94 km region, and for small isolated regions

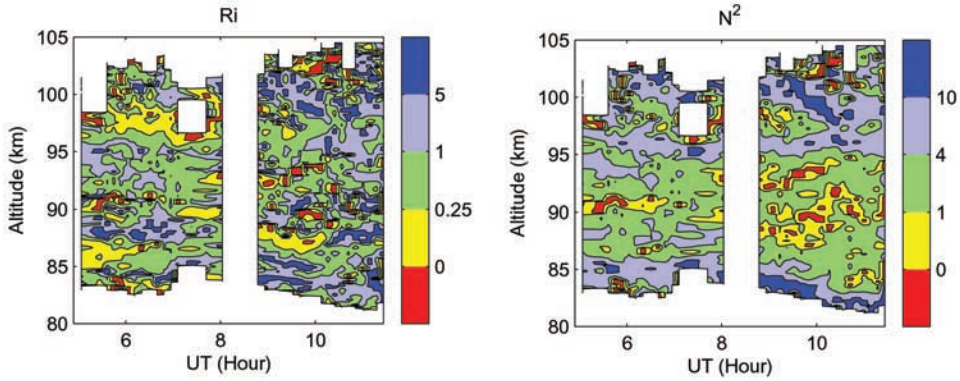

Figure 4. Contour plots for R_i and N^2 as a function of time and altitude from the data from positions P1 and P2. For the R_i data, yellow indicates a region of dynamical instability and orange a region of convective instability. For the N_2 data, orange represents regions of convective instability where N_2 was less than zero.

between 95 and 100 km. The Ri plots incorporate the wind shear as well as N^2. In addition to the isolated regions of convective instability below 95 km, a possible convective instability also existed just above 100 km although there are considerable uncertainties in the temperatures at those altitudes. More certain was the dynamical instability at 87 to 88 km and the narrow dynamical instability at 0930 UT just above 96 km. Much earlier (prior to 0900 UT) the 96 to 98 km region had undergone dynamical (and possibly convective) instability for a period of over an hour from 6 to 8 UT. This earlier instability is related to the convective rolls discussed by *Larsen et al.* [2004].

[30] The general picture that arises from these contour plots is as follows. Below 95 km much of the region from 86 to 94 km had been convectively unstable at some point for the period from 9 to 10 UT. When not convectively unstable it may have been dynamically unstable. At 10 UT active unstable regions (probably convectively, but possibly dynamically unstable) occurred around 90 and 93 km. The region from 87 to 88 km was more or less continuously dynamically unstable from 9 to 10 UT, although convective instabilities appeared briefly. The region from 95 to 98 km was dynamically unstable around 0930 UT. Earlier from 6 to 8 UT it had been dynamically (and possibly convectively) unstable. It was not unstable over a 1 km thick or larger region at the time of the launch, although it could have been at shorter scales. It is also possible that narrow regions went briefly convectively unstable. Above 100 km the region around 102 km may have been either convectively or dynamically unstable.

4. Results

4.1. TMA Observations

[31] Figure 5 shows the downleg trail (for which there are no lidar data) which shows scalloped KH billows

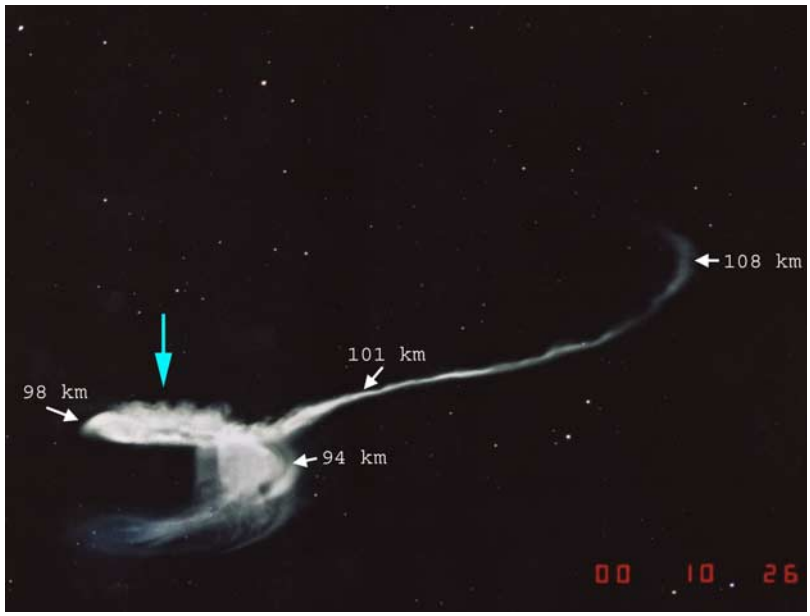

Figure 5. A photograph of the TMA trail on the downleg. The arrow points to the KH billows which occur between 96 and 99 km.

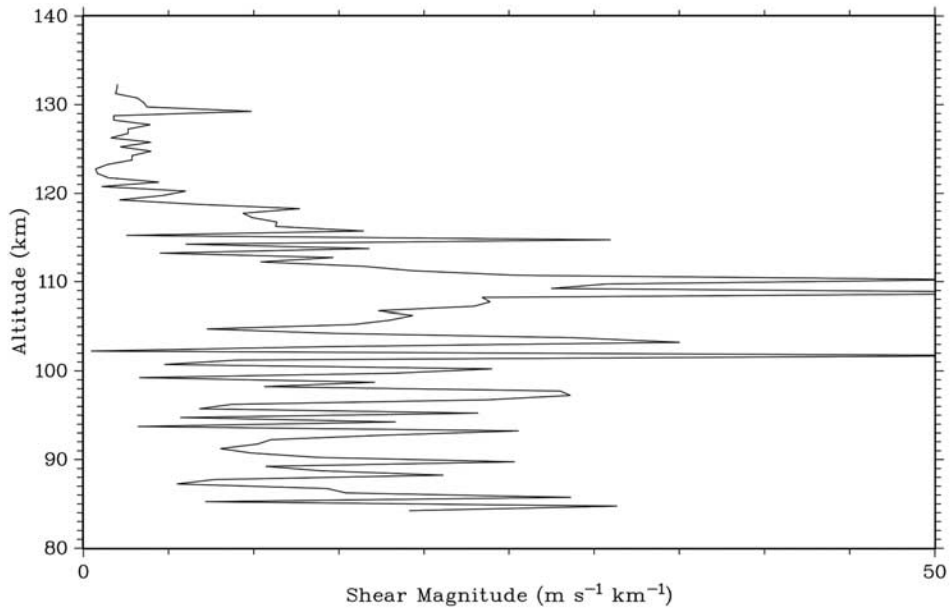

Figure 6. The shear magnitude as a function of altitude from the upleg TMA data.

between 96 and 99 km. The billow spacing is 5 km suggesting a thin unstable layer about 0.5 km in vertical extent [e.g., *Larsen*, 2000a]. The vertical extent of the billows is 3 km consistent with this spacing. Billows were less clearly seen but were present on the upleg from above 91 to below 96 km, at which point, the trail turned 45 degrees and billows appeared also from 96 to below 98 km. The billows from above 91 to below 96 km may be associated with the convective/dynamical instability seen in the Ri contour plot in Figure 4 at 93 km. Note that the lifetime of convective billows may be quite short [*Hecht et al.*, 1997] so that their absence on the downleg may not be unusual. The billows above 95 km on the upleg and downleg are associated with the large shear and the dynamical instability seen in the lidar data prior to 1000 UT. This instability had appeared to completely dissipate by the launch but because of its small vertical extent a 250 m unstable region would not be seen in the lidar plots which are smoothed over 1 km. Furthermore, simulations show the lifetime of KH billows to be on the order of a few tens of minutes [*Fritts et al.*, 1996] so that they could also be remnants from the earlier instability.

[32] *Larsen et al.* [2003] present an extensive comparison between the lidar-derived and TMA-derived meridional and zonal winds. The lidar was actually turned off just prior to the launch and did not turn on again until 1007 UT. Nevertheless there was overall excellent agreement between the two techniques. There were some differences but these are attributed to the horizontal averaging of the lidar beam and the changing geophysical conditions. In particular, the meridional wind shear above 95 km was decreasing throughout the launch period. The major difference was the smaller zonal shear measured by the TMA between 85 and 90 km. This feature was persistent in the lidar data, but because the lidar data needs two well-separated positions to derive the zonal winds small-scale structure will not be captured. The TMA winds are sensitive to small-scale structure so the differences at those altitudes strongly suggest the presence of localized small-scale features, not inconsistent perhaps with turbulent conditions.

[33] Figure 6 shows the shear magnitudes from the TMA for the upleg. The largest shear during the launch was just below 102 km. When combined with the lidar temperature data this region was dynamically unstable and possibly even convectively unstable. Additional large shears were seen below 110 km. Note that a large shear is not seen at 97 km. However, the lifetime of KH billows is on the order of 30 minutes [*Fritts et al.*, 1996] and thus they could have been produced prior to the launch.

[34] More details on these next results can be found in the work of *Bishop et al.* [2004] and the following is a summary of the main findings. The chemical release technique is also able to measure energy dissipation rates (and horizontal eddy diffusion) from the horizontal expansion of the trail [*Rees et al.*, 1972; *Lloyd et al.*, 1973; *Lübken*, 1993; *Lübken et al.*, 1994]. The results show large values through much of the 85 to 110 km region. Values of eddy diffusion ranged from 3×10^5 cm^2/s at 85 km to near 2×10^7 cm^2/s at 102 km. At altitudes below 95 km the peak energy dissipation rate was 0.1 W/kg at 87 km. The values at 85 and 93 km were between 0.03 and 0.09 W/kg. Between 95 and 102 km the energy dissipation rate was generally above 0.3 W/kg with a peak of near 0.9 W/kg at 100 km. As has been found before [*Lübken*, 1993; *Lübken et al.*, 1994], the in situ energy dissipation results from trails or chaff are much higher than nominal ion gauge results, which typically vary around a few tens of mW/kg in this altitude region [*Hocking*, 1999].

4.2. Photometer Observations

[35] More details on these results can be found in the work of *Hecht et al.* [2004] and the following is a summary of the main findings. The airglow volume emission profiles derived from the photometer data are shown in Figure 7. Both the O2 atmospheric (O2A) band and greenline emission were peaking near or below 90 km, quite different from

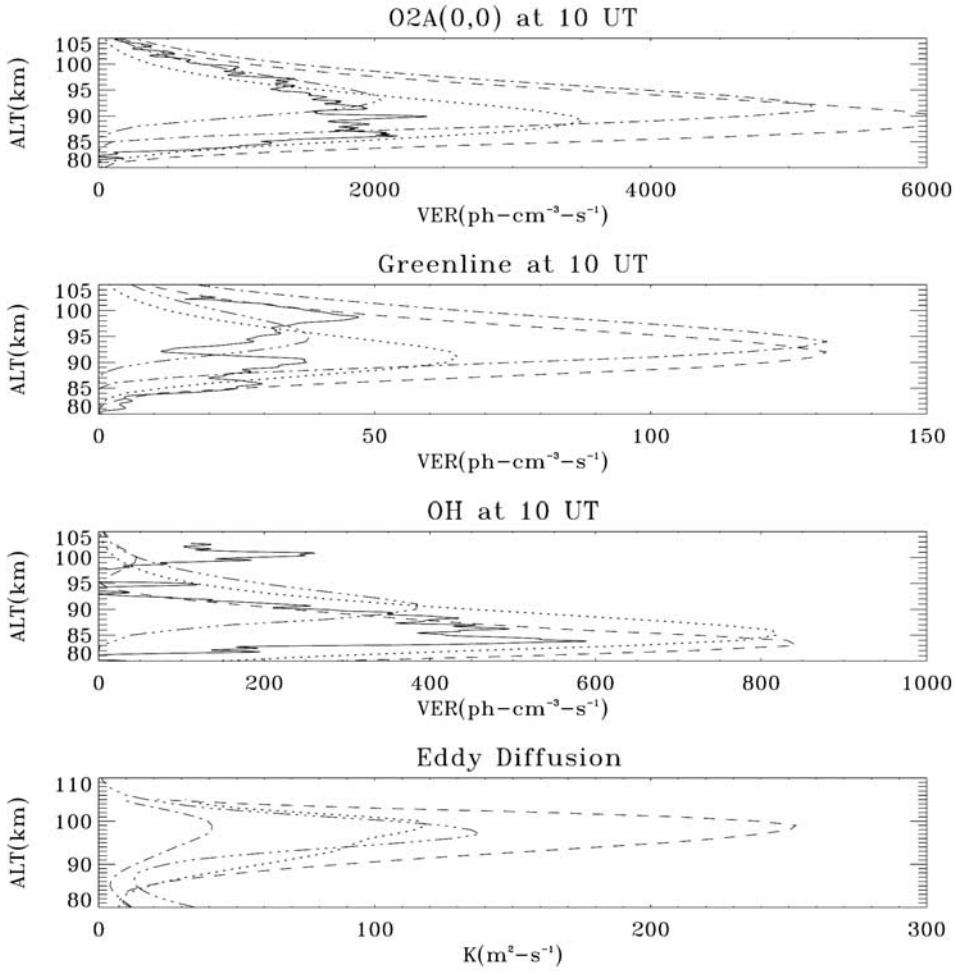

Figure 7. Three panels of airglow volume emission rates (VERs) and one panel of eddy diffusion. Each airglow panel also shows TIME-GCM model predictions of these VERs using different eddy diffusion profiles which are shown in the bottom panel. The line style of each model run corresponds to the line style of the eddy diffusion model. The first panel shows the measured O2A VER (solid line) versus altitude compared to four TIME-GCM predictions taken from *Hecht et al.* [2004]. The second panel is the same but for greenline. The third panel is the same but for OHM (9, 4). Here only three model predictions are shown. The fourth panel shows the four different eddy diffusion models used.

the model TIME-GCM results which are shown for different choices of eddy diffusion profiles also shown in Figure 7. The shape of the O2A profile was quite flat between 87 and 95 km. This was also different from those found in the Coqui Dos rocket experiment [*Hecht et al.*, 2000] where the O2A band peaked more nominally near 94 km. The airglow data were inverted and the resultant oxygen density [O] profile is quite different from the TIME-GCM model predictions. The profile is quite flat from 87 to 95 km although there is a peak at 90 km. There is also some structure in the profile around 97 km and at 102 km.

[36] If turbulence produced a mixing of the constituent profile this should show up in the oxygen mixing ratio which is the ratio of [O] to the total density. The total density was derived from the lidar temperature data and a single seed point at 103 km from the TIME-GCM. The result is shown as a heavy line in Figure 8 compared to a TIME GCM model result using the same total density and a TIME-GCM [O] profile. Clearly the observed mixing ratio is less dependent on altitude than the model in the 85 to 95 km region. This suggests that during the launch period there existed a well-mixed region, probably due to the convective instability present in this region over the prior hour. However, as discussed in the work of *Hecht et al.* [2004] an AGW or tide also can produce some altitude independence for the mixing ratio in this region since an AGW or tide can produce a fluctuation in the mixing ratio [*Walterscheid et al.*, 1987; *Walterscheid and Schubert*, 1995]. Modeling of the effect of an AGW or tide on the mixing ratio in the work of *Hecht et al.* [2004] suggests that an AGW or tide could have contributed to part of the observed mixing in the 86 to 95 km region.

[37] There was some structure in the profile, with peaks near 90 km (the region of the active convective instability at the time of the launch), around 97 km (the region of the KH billow), and around 102 km, the region of the unstable shear region seen in the TMA trail data. The Na density data also showed structure around 90 and an altitude-independent

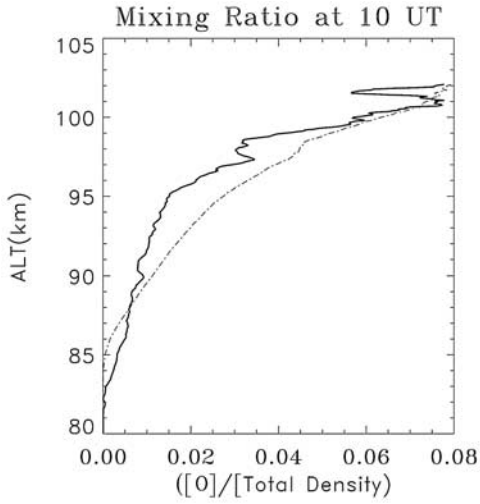

Figure 8. Two plots of the atomic oxygen mixing ratio [O]/[M] versus altitude, where [O] and [M] are the atomic oxygen and total densities respectively. The heavy solid line uses the measured [O] from the photometers while the thin dashed-dot line uses TIME-GCM model [O].

slope around 97 km. The short vertical wavelength of the structure around 90 km (1 km) makes it unlikely that it is an AGW.

[38] Interestingly, no structures were seen at 93 km or at 87–88 km. The 93 km convectively unstable region at the time of the launch appears to have been narrow (below 1 km based on the profiles taken closest to launch) and thus would not be resolved by the photometers. The lack of structure at 87–88 km is more interesting. Clearly the dominant effects on mixing ratio occurred over the 85 to 95 km altitude region, probably by some combination of wave activity and convective instability. The TOMEX results suggest one possibility; that the mixing due to the convective instability erased any signature of the mixing caused by the dynamical instability.

4.3. Ionization Gauge Observations

[39] The main results from the ionization gauge are summarized in Figure 9 which contains a profile of the fluctuations observed by the forward sensor during the upleg. These fluctuations are those present after any large-scale variations (above 1 km in vertical extent) are filtered out. The relative fluctuations were typically low when compared to some of the more turbulent regions measured by *Lübken et al.* [1994]. Following the methods of *Blix et al.* [1990], these levels correspond to dissipation rates of a few mW/kg at most. However, a large amount of structure was present, as peaks were observed to occur at 88 km, 101 km, and 108 km. Similar to the measurements of *Lehmacher and Lübken* [1995], the peaks were narrow (<100 m) in vertical extent. In addition to the structured peaks, generally higher levels of fluctuation were also observed in the range from 105 km to 110 km. These fluctuations seem to associate well with the wind shears observed in the TMA trails. In contrast, the ionization gauge registers little or no increase in fluctuations as the payload enters regions identified as convectively unstable from the lidar data. (That is, the region between 85 and 95 km exhibiting Richardson numbers near zero.) This situation is to be expected because, as noted by *Lübken* [1993] and *Lehmacher and Lübken* [1995] ionization gauges generally are not sensitive to the mixing caused by convective instabilities.

4.4. Tides and AGWs

[40] Under certain conditions the tidal amplitudes for temperatures can be quite significant at these altitudes. *Liu et al.* [2004] analyzed the data for the TOMEX night and the combined data for the observations from 26 October to 2 November with respect to the presence of 12 and 24 hour tides. They also compared the observed results with those derived from the TIME-GCM. They found that both tides have significant amplitude and may in fact be responsible for a significant fraction of the observed temperature perturbation seen around 90 km on 26 October. As such the diurnal tide produced much of the low stability due to the large temperature gradient seen around 90 km. The exact magnitude of this gradient however is affected, to a lesser extent, by the semidiurnal tide. Nevertheless, it cannot be ruled out that a large amplitude AGW with a period of several hours also caused part of the observed large temperature gradient near 90 km on the TOMEX night.

5. Discussion

[41] While the investigators for the individual TOMEX studies presented their conclusions about the parameters each instrument measured in the other papers of this section, here we would like to determine the effects of the various observed instabilities on the suite of measurements. Table 1 provides a summary of the results from the rocket measurements of billows, energy dissipation, neutral density fluctuations, and O mixing with respect to altitude and instabilities as measured by the lidar. The instability column

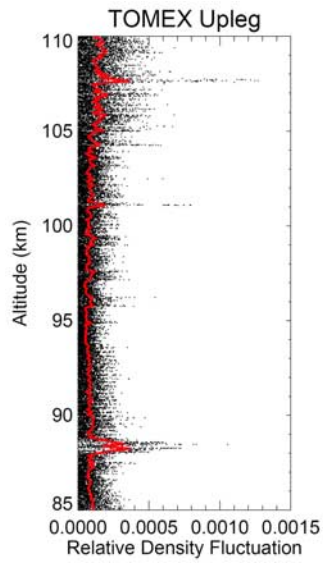

Figure 9. Relative density fluctuations observed by the forward ionization gauge sensor on the upleg. The large-scale atmospheric density has been removed so that only variations of vertical extent less than 1 km are shown. Individual measurements are plotted as black dots, while the red curve indicates a sliding average 0.5 km in width.

Table 1. Rocket Observations Versus Atmospheric Stability

Altitude, km	Instability[a,b,c]	Billows[d]	Energy Dissipation[e]	ND Fluctuations[e,f]	O Mixing[e]
86–94	convective(H)	some	moderate	low	high
87–88	dynamical(A)	none	local peak	peak	no peak
89–91	convective(A)	none	very low	low	peak
93	convective(A)	up	moderate	low	no peak
96–98	dynamical(A,H),over	up/down	high	low	peak
100–102	dynamical?(A),over	none	highest	peak	peak
105	largest winds(TMA)	none	high	no peak	no data
105–110	high shears(TMA)	none	high	increasing	no data

[a](H) refers to an historical instability that was present prior to launch.
[b](A) refers to an active instability that was present at the time of launch.
[c]Over refers to the overturning in Na density above 95 km that was present before the launch.
[d]Up and down refer to the upleg and downleg trajectories.
[e]Peak refers to an observed peak in the measured profiles.
[f]ND refers to neutral density.

indicates that almost the entire region above 85 km was either unstable or had been recently unstable. The following summarizes the various effects of the three types of observed instabilities.

5.1. Convective Instabilities

[42] Since the IG technique is not sensitive to fluctuations in regions where the temperature lapse rate is adiabatic it is not surprising that there was little evidence of enhanced fluctuations in the regions of convective instability. However, in contrast, the convective instability seems to have been the most effective mechanism for mixing as the [O]/(total density) mixing ratio suggests that the 86 to 94 km region was well-mixed. However, the presence of a large vertical wavelength AGW or a tide means that part of the mixing could have been be distorted by this wave as discussed in the photometer section above. The TMA results suggest moderately high energy dissipation in the 86–94 km region but those values are low compared to those found at higher altitudes where the overturning occurred. Billows were seen from 92 to 95 km on the upleg and these were probably associated with the active convective instability at 93 km. However, one of the regions where an active convective region is present (90 km) shows very low energy dissipation. Since the energy dissipation was determined from the TMA cloud expansion, it cannot be ruled out that this inferred low energy dissipation was being affected by turbulence induced by the active convective instability. In general, though, the convective instabilities seem to have an important effect over a large altitude range.

5.2. Dynamical Instabilities

[43] The dynamical instability had the most striking effect, the production of well-formed Kelvin-Helmholtz (KH) billows on the upleg and downleg just above 95 km. The instability layer at that altitude was recent and the KH billows had probably just formed. Since the lifetime of these structures is short (a few tens of minutes) there absence at 87 km is not problematical as that instability probably formed and decayed early in the period of unstable conditions. Interestingly, the highest value of energy dissipation below 95 km was found at 87 km. The dynamical instability also produced enhanced fluctuations in the IG measurements. In those data the fluctuations were confined to narrow layers, as has been seen by others. There was also a peak at 97 km in the [O] mixing ratio probably attributable to the recent dynamical instability. There was no peak in the mixing ratio at 87 km, but again the decay of that instability into turbulence had probably already occurred, and as that region was well-mixed already no additional effect would be expected to be seen. Compared to the effects of the convective instability, the effects of the dynamical instability seem to be confined to a narrow altitude regime. However, this confinement may be related to the presence of the convective roll overturning.

5.3. Overturning Near 100 km/Convective Rolls

[44] With respect to energy dissipation the largest effects occurred above 95 km with uniformly high results in the region from 96 to 102 km where the overturning, possible due to a convective roll, was observed to exist for many hours prior to the TOMEX launch. The peak value was nearly 10 W/kg, almost 15 times higher than that found below 95 km. Neither the IG data nor the [O] mixing ratio data however showed evidence of large-scale structure that would be associated with the overturning rather than with the more localized KH billows. However, at the time of the launch the region around 97 km, the region of the Na overturning was in the same region where the O was well-mixed. Therefore it is difficult to separate the effects of the overturning from that of the KH instability that also existed at that altitude.

5.4. TOMEX Data and Atmospheric Stability

[45] The picture that emerges from TOMEX is one where large regions of the 85 to 105 km region were close to instability for long periods of time. This was due to combined effects of tides and/or large vertical wavelength atmospheric gravity waves which together act to produce regions of near convective or dynamic instability. This is consistent with the picture previously presented in the work of *Gardner et al.* [2002] and *Zhao et al.* [2003]. With an atmosphere therefore near instability smaller vertical scale AGWs passing through the region can cause large regions to actually go unstable producing significant mixing and turbulence. Thus while at any one time only small regions may be going unstable the cumulative effect is to make a large region quickly turbulent and well-mixed.

[46] *Hodges* [1969] did anticipate that small amplitude AGWs could break and cause turbulence because of the lapse rate near the mesopause. The result from TOMEX, where instabilities can exist over a large vertical extent, is somewhat different from the more classical picture [e.g., *Hodges*, 1969; *Lindzen*, 1981] where mixing and turbulence are caused by AGWs growing large enough to break by themselves in a rather narrow restricted altitude region. However, the data were not available until recently from experiments such as TOMEX and other ground-based lidar results [*Gardner et al.*, 2002; *Zhao et al.*, 2003] to indicate how close the atmosphere is to instability, both with respect to large wind shears and large negative temperature gradients.

6. Conclusions

[47] The TOMEX experiment was designed to study how instabilities affect the dynamics and structure of the 80 to 110 km region. With respect to the mixing of atmospheric constituents it appears that the large vertically extensive convective instability had the greatest effect in producing a nearly well-mixed region over nearly 10 km. However, a large AGW or tide which caused that instability may have also partly distorted the observed [O] mixing. By contrast, the dynamical instabilities had a more limited effect producing narrower regions of mixing. The large overturning event, the cause of which is suggested by *Larsen et al.* [2004] as being due to a new type of process at these altitudes, convective rolls, seems to have had a much less identifiable effect on the atmospheric structure. While the energy dissipation as measured by the TMA was enhanced below 95 km, presumably due to the combined effects of convective and dynamical instabilities, the largest values were associated with the region of the persistent Na density overturning. The TOMEX results are consistent with recent data such as those presented by *Gardner et al.* [2002] suggesting that large vertical regions near the mesopause are often close to instability. With the atmosphere above 80 km being close to instability as was observed during TOMEX, only small additional perturbations are needed to cause an instability to form with its subsequent turbulence, energy dissipation, and eddy mixing. Given these results, it would be desirable to have a series of launches that focused on the evolution of each type of instability separately.

[48] **Acknowledgments.** The Aerospace results could not have been obtained without the invaluable help given by Paul Carranza and Mike Ben-Ami. JHH, RLW, and JHC were supported by NASA grant NAG5-5235, and by the Aerospace IR and D program. MFL and RLB acknowledge partial support from NASA grant NAG5-5242 and NSF grant ATM-0003168. AZL, GRS, and CSG acknowledge the support from NASA grant NAG 5-5241.

References

Angelats i Coll, M., and J. M. Forbes (1998), Dynamical influences on atomic oxygen and 5577 Å emission rates in the lower thermosphere, *Geophys. Res. Lett.*, *25*, 461–464.

Bills, R. E., C. S. Gardner, and S. F. Franke (1991), Na Doppler/temperature lidar: Initial mesopause region observations and comparisons with the Urbana MF radar, *J. Geophys. Res.*, *96*, 22,701–22,707.

Bishop, R. L., M. F. Larsen, J. H. Hecht, A. Z. Liu, and C. S. Gardner (2004), TOMEX: Mesospheric and lower thermospheric diffusivities and instability layers, *J. Geophys. Res.*, *109*, D02S03, doi:10.1029/2002JD003079, in press.

Blix, T. A., E. V. Thrane, and Ø. Andreassen (1990), In situ measurements of the fine structure and turbulence in the mesosphere and lower thermosphere by means of electrostatic ion probes, *J. Geophys. Res.*, *95*, 5533–5548.

Chamberlain, J. W. (1961), *Physics of the Aurora and Airglow*, 456 pp., Elsevier Sci., New York.

Coble, M. R. (1997), Computing two-dimensional unambiguous horizontal wave number spectra from OH airglow images, Ph.D. dissertation, Univ. of Ill., Urbana-Champaign.

Coble, M. R., G. C. Papen, and C. S. Gardner (1998), Computing two-dimensional unambiguous horizontal wavenumber spectra from OH airglow images, *IEEE Trans. Geosci. Remote Sens.*, *36*, 368–382.

Friker, A., and F.-J. Lübken (1992), Neutral air density and temperature measurements by the TOTAL instrument aboard the ROSE payload, *J. Atmos. Terr. Phys.*, *54*, 693–701.

Fritts, D. C., and T. J. Dunkerton (1985), Fluxes of heat and constituents due to convectively unstable gravity waves, *J. Atmos. Sci.*, *42*, 549–556.

Fritts, D. C., T. L. Palmer, Ø. Andreassen, and L. Lie (1996), Evolution and breakdown of Kelvin-Helmholtz billows in stratified compressible flows. part 1: Comparison of two- and three-dimensional flows, *J. Atmos. Sci.*, *53*, 3173–3191.

Fritts, D. C., J. R. Isler, J. H. Hecht, R. L. Walterscheid, and Ø. Andreassen (1997), Wave breaking signatures in OH airglow and sodium densities and temperatures: 2. Simulation of waves and instability structures, *J. Geophys. Res.*, *102*, 6669–6684.

Garcia, R. R., and S. Solomon (1985), The effect of breaking gravity waves on the dynamics and chemical composition of the mesosphere and lower thermosphere, *J. Geophys. Res.*, *90*, 3850–3868.

Gardner, C. S., and G. C. Papen (1995), Mesospheric Na wind/temperature lidar, *Rev. Laser Eng.*, *23*, 131–134.

Gardner, C. S., K. Galati, Y. Zhao, and G. Swenson (1999), Measuring gravity wave momentum and fluxes with airglow images, *J. Geophys. Res.*, *104*, 11,903–11,915.

Gardner, C. S., Y. Zhao, and A. Z. Liu (2002), Atmospheric stability and gravity wave dissipation in the mesopause region, *J. Atmos. Sol. Terr. Phys.*, *64*, 923–929.

Gossard, E. E., and W. H. Hooke (1975), *Waves in the Atmosphere, Atmospheric Infrasound and Gravity Waves—Their Generation and Propagation*, 456 pp., Elsevier Sci., New York.

Hagan, M. E., and J. M. Forbes (2002), Migrating and nonmigrating diurnal tides in the middle and upper atmosphere excited by tropospheric latent heat release, *J. Geophys. Res.*, *107*(D24), 4754, doi:10.1029/2001JD001236.

Haque, R., and G. R. Swenson (1999), Extraction of motion parameters of gravity-wave structures from all-sky OH image sequences, *Appl. Opt.*, *38*, 4433–4442.

Hecht, J. H., R. L. Walterscheid, D. C. Fritts, J. R. Isler, D. C. Senft, C. S. Gardner, and S. J. Franke (1997), Wave breaking signatures in OH airglow and sodium densities and temperatures: 1. Airglow imaging, Na lidar, and MF radar observations, *J. Geophys. Res.*, *102*, 6655–6668.

Hecht, J. H., S. Collins, C. Kruschwitz, M. C. Kelley, R. G. Roble, and R. L. Walterscheid (2000), The excitation of the Na airglow from Coqui Dos rocket and ground-based observations, *Geophys. Res. Lett.*, *27*, 453–456.

Hecht, J. H., A. Z. Liu, R. L. Walterscheid, R. Roble, M. F. Larsen, and J. H. Clemmons (2004), Airglow emissions and oxygen mixing ratios from the photometer experiment on TOMEX, *J. Geophys. Res.*, *109*, D02S05, doi:10.1029/2002JD003035, in press.

Hickey, M. P., and R. L. Walterscheid (2001), Secular variations of OI (5577) Åairglow in the mesopause region induced by transient wave packets, *Geophys. Res. Lett.*, *28*, 701–704.

Hickey, M. P., R. L. Walterscheid, and P. G. Richards (2000), Secular variations of atomic oxygen in the mesopause region induced by transient gravity wave packets, *Geophys. Res. Lett.*, *27*, 3599–3602.

Hillert, W., F.-J. Lübken, and G. Lehmacher (1994), TOTAL: A rocket-borne instrument for high resolution measurements of neutral air turbulence during DYANA, *J. Atmos. Terr. Phys.*, *54*, 1835–1852.

Hocking, W. K. (1999), The dynamical parameters of turbulence theory as they apply to middle atmosphere studies, *Earth Planet Space*, *51*, 525–541.

Hodges, R. R., Jr. (1967), Generation of turbulence in the upper atmosphere by internal gravity waves, *J. Geophys. Res.*, *72*, 3455–3458.

Hodges, R. R., Jr. (1969), Eddy diffusion coefficients due to instabilities in internal gravity waves, *J. Geophys. Res.*, *74*, 4087–4090.

Larsen, M. F. (2000a), A shear instability seeding mechanism for quasi-periodic radar echoes, *J. Geophys. Res.*, *105*, 24,931–24,940.

Larsen, M. F. (2000b), Coqui 2: Mesospheric and lower thermospheric wind observations over Puerto Rico, *Geophys. Res. Lett*, *27*, 445–448.

Larsen, M. F. (2002), Winds and shears in the mesosphere and lower thermosphere: Results from four decades of chemical release wind measurements, *J. Geophys. Res.*, *107*(A8), 1215, doi:10.1029/2001JA000218.

Larsen, M. F., I. S. Mikkelsen, J. W. Meriwether, R. Niciejewski, and K. Vickery (1989), Simultaneous observations of neutral winds and electric fields at spaced locations in the dawn auroral oval, *J. Geophys. Res.*, *94*, 17,235–17,243.

Larsen, M. F., A. Z. Liu, R. L. Bishop, and J. H. Hecht (2003), TOMEX: A comparison of lidar and sounding rocket chemical tracer wind measurements, *Geophys. Res. Lett.*, *30*(7), 1375, doi:10.1029/2002GL015678.

Larsen, M. F., A. Z. Liu, C. S. Gardner, M. C. Kelley, S. Collins, J. Friedman, and J. H. Hecht (2004), Observations of overturning in the upper mesosphere and lower thermosphere, *J. Geophys. Res.*, *109*, D02S04, doi:10.1029/2002JD003067, in press.

Lehmacher, G., and F.-J. Lübken (1995), Simultaneous observation of convective adjustment and turbulence generation in the mesosphere, *Geophys. Res. Lett.*, *22*, 2477–2480.

Lindzen, R. S. (1981), Turbulence and stress due to gravity waves and tidal breakdown, *J. Geophys. Res.*, *86*, 9707–9714.

Liu, A. Z., R. G. Roble, J. H. Hecht, M. F. Larsen, and C. S. Gardner (2004), Unstable layers in the mesopause region observed with Na lidar during the Turbulent Oxygen Mixing Experiment (TOMEX) campaign, *J. Geophys. Res.*, *109*, D02S02, doi:10.1029/2002JD003056, in press.

Lloyd, K. H., C. H. Low, and R. A. Vincent (1973), Turbulence, billows, and gravity waves in a high shear region of the upper atmosphere, *Planet. Space Sci.*, *21*, 653–661.

Lübken, F.-J. (1993), Experimental results on the role of turbulence for the heat budget of the upper atmosphere, Hab. dissertation, Bonn Univ., Bonn, Germany.

Lübken, F.-J., U. von Zahn, E. B. Thrane, T. Blix, G. A. Kokin, and S. V. Pachomov (1987), In situ measurements of turbulent energy dissipation rates and eddy diffusion coefficients during MAP/WINE, *J. Atmos. Terr. Phys.*, *49*, 763–775.

Lübken, F.-J., W. Hillert, G. Lehmacher, U. von Zahn, T. A. Blix, E. V. Thrane, H.-U. Widdel, G. A. Kokins, and A. K. Knyazev (1994), Morphology and sources of turbulence in the mesosphere during DYANA, *J. Atmos. Terr. Phys.*, *56*, 1809–1833.

McDade, I. C., D. P. Murtaugh, R. G. H. Greer, P. H. G. Dickinson, G. Witt, J. Stegman, E. J. Llewellyn, L. Thomas, and D. B. Jenkins (1986), ETON 2: Quenching parameters for the proposed precursors of $O2(b^1\Sigma_g^+)$ and $O(^1S)$ in the terrestrial nightglow, *Planet. Space Sci.*, *34*, 789–800.

Mies, F. H. (1974), Calculated vibrational transition probabilities of $OH(X^2\Pi)$, *J. Molec. Spectrosc.*, *53*, 150–188.

Offermann, D. (1994), The DYANA campaign: A survey, *J. Atmos. Terr. Phys.*, *56*, 1639–1657.

Rees, D., R. G. Roper, K. H. Lloyd, and C. H. Low (1972), Determination of the structure of the atmosphere between 90 and 250 km by means of contaminant releases at Woomera, May 1968, *Philos. Trans. R. Soc. London*, *271*, 631–666.

Richardson, L. F. (1920), The supply of energy from and to atmospheric eddies, *Proc. R. Soc. London, Ser. A*, *67*, 354–373.

Roble, R. G., and E. C. Ridley (1994), A thermosphere ionosphere mesosphere electrodynamics general circulation model (TIME-GCM): Equinox solar cycle minimum simulation (30–500 km), *Geophys. Res. Lett.*, *21*, 417–420.

Rose, G., et al. (1992), The ROSE project, scientific objectives and preliminary discussion of results, *J. Atmos. Terr. Phys.*, *54*, 657–667.

Schoeberl, M. R., D. F. Strobel, and J. P. Apruzese (1983), A numerical model of gravity wave breaking and stress in the mesosphere, *J. Geophys. Res.*, *88*, 5249–5259.

Swenson, G. R., R. Haque, W. Yang, and C. S. Gardner (1999), Momentum and energy fluxes of monochromatic gravity waves observed by an OH imager at Starfire Optical Range, New Mexico, *J. Geophys. Res.*, *104*, 6067–6080.

Thrane, E. V., T. A. Blix, C. Hall, T. L. Hansen, U. von Zahn, W. Meyer, P. Czechowsky, G. Schmidt, H.-U. Widdel, and A. Neumann (1987), Small scale structure and turbulence in the mesosphere and lower thermosphere at high altitudes in winter, *J. Atmos. Terr. Phys.*, *49*, 751–762.

Thrane, E. V., T. A. Blix, U.-P. Hoppe, F.-J. Lübken, W. Hillert, G. Lehmacher, and D. C. Fritts (1994), A study of small-scale waves and turbulence in the mesosphere using simultaneous in situ observations of neutral gas and plasma fluctuations, *J. Atmos. Terr. Phys.*, *56*, 1797–1808.

von Zahn, U. (1987), The project MAP/WINE: An overview, *J. Atmos. Terr. Phys.*, *49*, 607–620.

von Zahn, U., F.-J. Lübken, and C. Putz (1990), BUGATTI experiments: Mass spectrometric studies of lower thermosphere eddy mixing and turbulence, *J. Geophys. Res.*, *95*, 7443–7465.

Walterscheid, R. L., and G. Schubert (1995), Dynamical-chemical model of fluctuations in the OH airglow driven by migrating tides, stationary tides, and planetary waves, *J. Geophys. Res.*, *100*, 17,443–17,450.

Walterscheid, R. L., G. Schubert, and J. M. Straus (1987), A dynamical-chemical model of wave-driven fluctuations in the OH nightglow, *J. Geophys. Res.*, *92*, 1241–1254.

Zhao, Y., A. Z. Liu, and C. S. Gardner (2003), Measurements of atmospheric stability in the mesopause region at Starfire Optical Range, NM, *J. Atmos. Sol. Terr. Phys.*, *65*, 219–232.

R. L. Bishop and M. F. Larsen, Department of Physics, Clemson University, Clemson, SC 29634, USA. (rbishop@clemson.edu; mlarsen@clemson.edu)

J. H. Clemmons, J. H. Hecht, and R. L. Walterscheid, Space Science Applications Laboratory, The Aerospace Corporation, M2-259, P. O. Box 92957, Los Angeles, CA 90009, USA. (james.clemmons@aero.org; james.hecht@aero.org; richard.walterscheid@aero.org)

C. S. Gardner, A. Z. Liu, and G. R. Swenson, Department of Electrical and Computer Engineering, University of Illinois, 308 C.S.L., 1308 W. Main Street, Urbana, IL 61801, USA. (cgardner@uiuc.edu; liuzr@uiuc.edu; swenson1@uiuc.edu)

R. G. Roble, National Center for Atmospheric Research, Boulder, CO 80307, USA. (roble@hao.ucar.edu)